analytical chemistry

pubs.acs.org/ac Article

Membrane-Based *In Situ* Mid-Infrared Spectroscopic Ellipsometry: A Study on the Membrane Affinity of Polylactide-*co*-glycolide Nanoparticulate Systems

Alekszej Romanenko, Benjamin Kalas, Petra Hermann, Orsolya Hakkel, Levente Illés, Miklós Fried, Peter Fürjes, Gergö Gyulai, and Peter Petrik*

Cite This: https://dx.doi.org/10.1021/acs.analchem.0c03763 Read Online

ACCESS | Metrics & More | Article Recommendations

ABSTRACT: Mid-infrared (IR) ellipsometry of thin films and molecule layers at solid−liquid interfaces has been a challenge because of the absorption of light in water. It has been usually overcome by using configurations utilizing illumination through the solid substrate. However, the access to the solid−liquid interface in a broad spectral range is also challenging due to the limited transparency of most structural materials in the IR wavelength range. In this work, we propose a concept of a microfabricated analysis cell based on an IR-transparent Si membrane with advantages of a robust design, flexible adaptation to existing equipment, small volume, multiple-angle capabilities, broad wavelength range, and opportunities of multilayer applications for adjusted ranges of high sensitivity. The chamber was prepared by 3D micromachining technology utilizing deep reactive ion etching of a silicon-on-insulator wafer and bonded to a polydimethylsiloxane microfluidic injection system resulting in a cell volume of approximately 50 μL. The mechanical stability of the 2 and 5 μm-thick membranes was tested using different "backbone" reinforcement structures. It was proved that the 5 μm-thick membranes are stable at lateral cell sizes of 5 mm by 20 mm. The cell provides good intensity and adjustment capabilities on the stage of a commercial mid-IR ellipsometer. The membrane configuration also provides optical access to the sensing interfaces at a broad range of incident angles, which is a significant advantage in many potential sensing structure configurations, such as plasmonic, multilayer, 2D, or metamaterial applications.

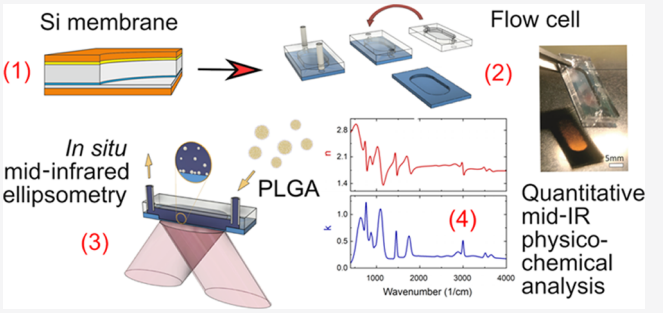

INTRODUCTION

In situ mid-infrared (IR) spectroscopy at solid−liquid interfaces requires special configurations such as that of[1] utilizing the "mirage" effect or the attenuated total internal reflection method.[2] Mid-infrared spectroscopic ellipsometry (IRSE),[3,4] primarily used in *ex situ* configurations[5] revealing nanometer sensitivity,[6] adds supplementary quantitative information to conventional spectroscopic results, such as layer thicknesses, volume fractions of constituents, lateral and vertical distributions (such as carrier depth profiles[7]), and optical anisotropy.[8] IRSE is a sensitive tool to measure chemical information in many fields including Si[9] and polymer technology.[10] The power of spectroscopic ellipsometry (SE) is that its sensitivity is comparable to interferometric methods; however, it does not need coherent sources and so stringent requirements neither in terms of alignment nor mechanical and temperature stability.

The instrumentation of ellipsometry is mature for most configurations, including IRSE.[10] The wavelength range from 1600 to 30,000 nm is already covered by most manufacturers, which extends the range of the deep ultraviolet−visible−near infrared ellipsometry of ≈200−2000 nm. Due to the light absorption of typical (water-based) samples in the IR wavelength range, the access to solid−liquid interfaces is only possible from the substrate side. The applicability of materials is limited because there are only a few that are transparent in such a broad wavelength range (Figure 1). Numerous practical considerations (such as fragility or water solubility) also play an important role in selecting a proper material.

Using Si wafers in a wedge-shaped cut[11,12] or a Kretschmann arrangement[13] can be an excellent solution for sensing purposes, although the absorption of Si limits the applicable spectral region (Figure 1). In this work we show that, by

Received: September 4, 2020
Accepted: December 2, 2020

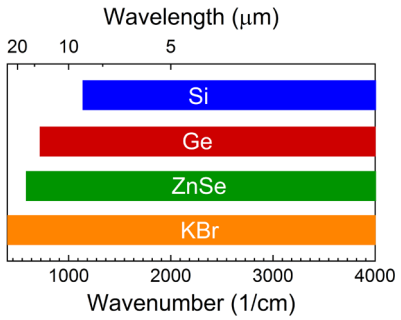

Figure 1. Transparent spectral ranges for Si, Ge, ZnSe, and KBr.

applying a micromachined microliter-volume Si flow cell, the wavelength range up to 25 μm or above is available due to the thin membranes, primarily only limited by the cutoff by the detection and illumination of the used ellipsometer. It is also important to emphasize that the method can easily be integrated in any commercial or homemade instruments.

In the wedge-shape construction, the two planes of the flow cell facing inside and outside are not parallel; hence, the beam reflected from the outside plane leaves the system in an off-axis direction and does not reach the detector. In the case of our self-designed 50 μL flow cell, the 2 and 5 μm-thick membranes are part of the optical model because the planes at the incidence and sensing surfaces are parallel. We show that the system with the membrane and the underlying liquid and interface layer can be measured and modeled accurately, and IRSE can be applied to analyze the interface layer in this configuration. We characterized the adsorption kinetics of poly(lactide-*co*-glycolides) (PLGA) onto the surface of the Si membrane using IRSE verified by a spectroscopic ellipsometer in the visible range, atomic force microscopy (AFM), and dynamic light scattering (DLS) to demonstrate the capabilities of the setup.

EXPERIMENTAL SECTION

Preparation of PLGA Nanoparticulate Systems. PLGA particles in the size range of 70−120 nm were prepared by using the nanoprecipitation method.[14,15] A 50 mg solution of PLGA50 (Sigma-Aldrich) was briefly dissolved in 5 mL of acetone solvent. The organic solution was then slowly added to 50 mL of doubly distilled water containing 50 mg of stabilizer (Pluronic 123, Sigma-Aldrich) by an automated pump under continuous stirring. Subsequently, the acetone solvent was evaporated overnight. The excess Pluronic was removed by centrifuging the solvent three times at 12,000*g* and exchanging

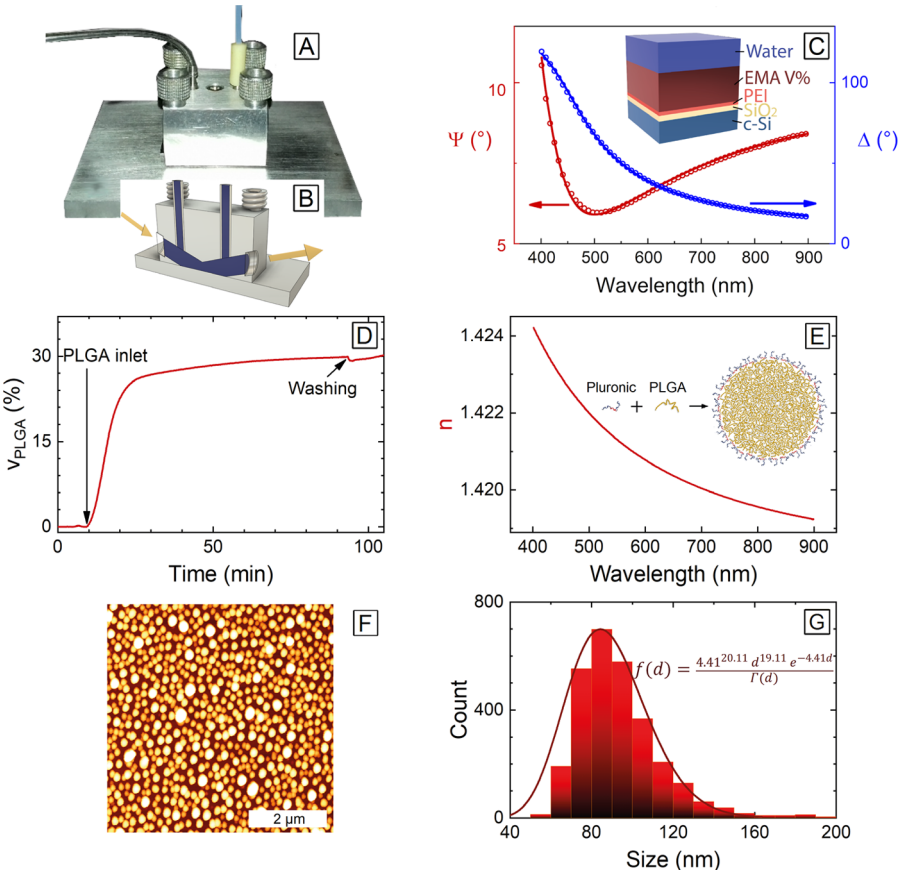

Figure 2. Photograph [A] and schematic view [B] of the conventional flow cell used for the reference measurements on a Si wafer at a fixed angle of incidence of 75°. [C] Measured (symbols) and fitted (lines) Ψ and Δ ellipsometry spectra after PLGA adsorption. The inset shows the optical model, in which c-Si denotes the substrate. [D] Volume fraction of PLGA nanoparticles (V_{PLGA}) adsorbed at a PEI-covered surface of a Si wafer measured in a conventional flow cell. The inlets of PLGA and MQ water for washing are shown by the arrows. [E] Dispersion of *n* determined from the evaluation shown in subfigure [C]. [F] AFM image on the nanoparticles attached to the surface of a Si wafer. The height scale from the darkest to the brightest pixels ranges from 0 to 130 nm. [G] Size distribution of the PLGA nanoparticles determined from the AFM image and the fitted curve. The structure of the PLGA nanoparticles is shown in the inset of graph [E].

https://dx.doi.org/10.1021/acs.analchem.0c03763
Anal. Chem. XXXX, XXX, XXX−XXX

the supernatant for doubly distilled water. The structure of the resulting PLGA nanoparticle is shown in Figure 2.

Spectroscopic Ellipsometry in the Visible Wavelength Range. A Woollam M-2000DI rotating compensator spectroscopic ellipsometer was used in the wavelength range from 400 to 900 nm. In this setup, the angle of incidence can generally be varied between 45° and 90°; however, a conventional flow cell is usually designed for a fixed angle of incidence that provides the highest sensitivity for a certain substrate and layer system.[16]

From an SE measurement, the amplitude ratio and the phase difference between the p- and s-polarized lights are provided, referring to them as Ψ and Δ ellipsometric angles, respectively. Then, the complex reflectance ratio can be calculated using the expression of $\rho = \tan(\Psi) \cdot \exp(i\Delta)$. By building an appropriate optical model consisting of all the layers present in the structure, their optical properties and thicknesses can be calculated.

The ellipsometer records a spectrum within several seconds, giving access to a large amount of data with adequate time resolution. Consequently, at each temporal point, a complex model can be used to reconstruct the change of the structure under investigation.

***In Situ* Measurement of PLGA Adsorption in a Conventional Flow Cell in the Near-Infrared to Near-Ultraviolet Wavelength Range.** The reference measurements were carried out in a traditional flow cell on Si wafers covered by a native oxide layer. The Si wafer was rinsed with high-purity Milli-Q (MQ) water before the measurement. To achieve a better PLGA adsorption, a polyethylenimine (PEI) solution was dripped onto the surface at a concentration of 0.5 mg/mL with a subsequent MQ water wash after 1 min. The PEI layer was prepared *ex situ* to avoid PLGA depletion during the *in situ* experiment caused by the PEI coverage at the tubes and at the wall of the flow cell. The samples were measured both before and after the adsorption of PEI in order to construct a better optical model together with proper references.

In the traditional flow cell configuration, the PLGA adsorption was measured at a fixed angle of incidence of 75° optimized for the Brewster angle of the optical system under investigation (Figure 2A,B). A continuous flow of 1 μL/s was provided by a peristaltic pump. The Δ offset caused by the stress in the windows of the flow cell was calibrated by measuring a known reference sample.

Figure 2C shows the measured spectra and the optical model that consists of water[17] as the ambient as well as an interface layer between the water and the PEI layer (denoted by "EMA" in Figure 2C), the PEI layer itself, the native oxide layer ("SiO_2" in the figure), and single-crystalline Si ("c-Si") as a substrate. "EMA" stands for the effective medium approximation,[18] an optical composition of volume fractions of ambient and PLGA (V_{PLGA}). According to previous investigations, the dispersion of the PEI layer was described using the Cauchy model of $n = 1.45 + 0.01/\lambda^2$, where λ stands for the wavelength of light in μm. The references of SiO_2 and c-Si are from ref 19.

Mid-Infrared Ellipsometry. IRSE has already been a well-spread method in terms of both instrumentation and interpretation. The spectral range that can typically be covered spans from ≈350 to 5000 1/cm (ca. between 2000 and 30,000 nm). Thus, by applying both instruments of SE and IRSE a wavelength range from 190 nm to 30,000 nm can be used. The instrument of this work was a Woollam IR-VASE Mark II ellipsometer in the spectral range of 330−6000 1/cm. To find a proper compromise between the spectral resolution and the signal-to-noise ratio, the resolution was selected to be 8 1/cm. The angle of incidence used during the membrane-based measurement was 53°, which was also a result of trade-off considerations between the spot size (less than 5 mm by 20 mm), the sensitivity, and the intensity.

Dynamic Light Scattering. Nanoparticle size was measured using dynamic light scattering (LS Instruments, NanoLab 3D). The experiments were carried out in 3D cross-correlation mode. Second-order cumulant analysis was performed to determine the average size and polydispersity. According to DLS measurements, the prepared nanoparticles had an average hydrodynamic diameter of (120 ± 10) nm with a polydispersity of 0.08 ± 0.01.

Atomic Force Microscopy. The morphology of the adsorbed PLGA nanoparticles was investigated by AFM using a XE-100 (Psia, South Korea) system. Measurements were carried out in non-contact mode utilizing NSC15 (Micromash, Estonia) cantilevers. Images were collected at 10 randomly selected locations with a typical scan area of 5 μm × 5 μm.

RESULTS

Monitoring of PLGA Adsorption in a Conventional Flow Cell. The adsorption of the PLGA nanoparticles was investigated by *in situ* optical monitoring in the flow cell using SE. The spectrum was acquired with a temporal resolution of 8 s. After achieving a stable baseline by flowing pure MQ water, the PLGA dispersion (0.5 mg/mL) was introduced for 90 min, which subsequently was followed by a washing step using MQ water again (Figure 2). The volume fraction of PLGA particles V_{PLGA}, the thickness of the EMA layer, and the dispersion of n were fitted after the *in situ* measurement. Thereafter, the thickness and the dispersion of n were fixed and used to determine the *in situ* V_{PLGA} values. Both the V_{PLGA} = 30% (Figure 2A) and n (Figure 2B) are close to the values reported in ref 20, although the dispersion of polymers strongly depends on the preparation and type.[21]

The change in V_{PLGA} was not significant during the washing process, showing that the adsorbed particles did not get washed off, also supported by the AFM images (Figure 2F). The small fluctuation of V_{PLGA} after washing can be explained by the difference in the refractive indices (n) of the liquid with particles and without particles, and the small pit in the initial stage (on the baseline close to the point shown by the arrow of "PLGA inlet") can be attributed to the mixing of the two media. The size distribution of the PLGA nanoparticles (Figure 2G) determined from the AFM confirmed the thickness of 81.6 ± 0.4 nm obtained by an SE.

Microfabrication of a Membrane-Based Flow Cell for IRSE. Dedicated flow chambers were designed and fabricated by 3D micromachining technology to be compatible with the applied IR ellipsometric characterization method. The structural material of the chamber was selected to be c-Si to ensure adequate transparency of the optical window formed by a thin (2−5 μm) Si membrane. The lateral dimensions of the chamber were defined by the optical configuration of the IR ellipsometric instrument and the required sample volume. Accordingly, an ellipsoidal chamber was formed with 5 and 20 mm characteristic axis lengths. A silicon-on-insulator (SOI) wafer provided by the Siegert Wafer GmbH and manufactured

https://dx.doi.org/10.1021/acs.analchem.0c03763
Anal. Chem. XXXX, XXX, XXX−XXX

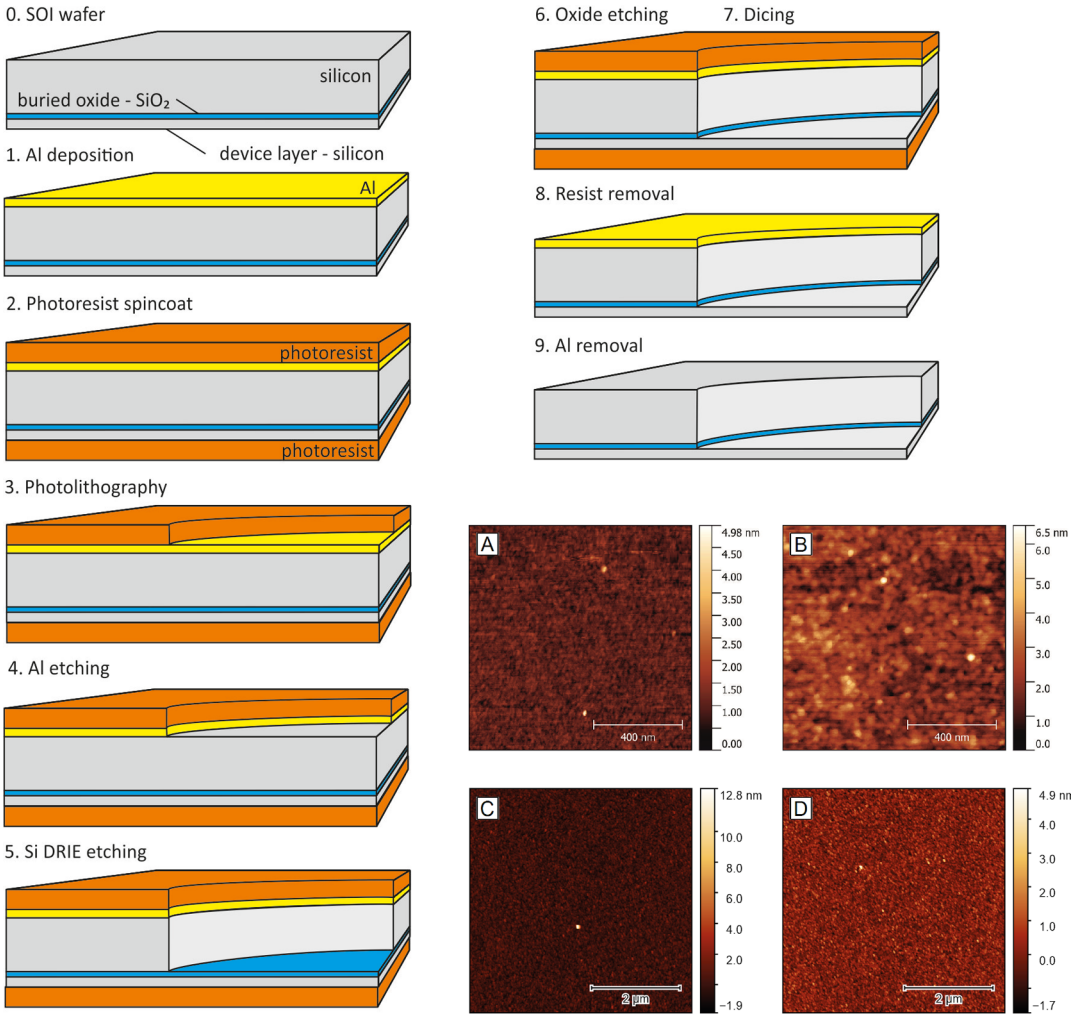

Figure 3. Process steps for fabrication of the silicon flow chamber by 3D micromachining of SOI wafer resulting in a few micrometer thin crystalline silicon membrane transparent in the IR spectral range: 1. Al deposition; 2 and 3. Photolithography; 4. Al etching; 5. Si DRIE; 6. Oxide etching; 7. Dicing; 8 and 9. Photoresist and Al removal. Surface maps of the silicon membrane of the flow cell measured by AFM are shown in images [A]−[D]. The root mean square roughness of the top [A] and buried [B−D] sides of the membrane are 0.25, 0.65, 0.53, and 0.40 with an accuracy of ≈0.1 nm, respectively.

by fusion bonding method[22] with subsequent grounding and polishing was used as initial substrate with 520 μm handle wafer thickness (as the chamber depth), 1 μm buried oxide thickness (as the etch stop layer), and 2−5 μm device layer thickness (as the membrane). Accordingly, the chamber volume was calculated to be ≈50 μL. The manufacturing technology of SOI wafers, especially fusion bonding as in our case, ensures device-quality, single-crystalline membranes.[23,24] The chamber was fabricated by using conventional 3D micromachining technology steps, see Figure 3. After the SOI substrate was cleaned, a 300 nm-thick Al layer was deposited on the back side of the wafer by vacuum evaporation (AJA ATC 1800 T UHV, Scituate, MA, USA). An adequate lateral pattern of the chamber was defined by conventional photolithography (Süss Microtec MA6, Garching, Germany), and the Al layer was selectively removed by wet etching. The chamber was prepared by highly anisotropic deep reactive ion etching (DRIE, Oxford Plasmalab 100 ICP 180, Bristol, UK) using the Bosch process practically stopped at the buried oxide (BOX) layer. The wafer was diced by a dicing saw (Disco DAD 320, Tokio, Japan), and the photoresist, Al, and silicon oxide layers were removed by wet chemistry subsequently.

The sample injection microfluidic system was designed to be compatible with the analysis chamber and fabricated by the soft lithography technique. The molding form of the channel systems was structured by photolithography using an SU-8 2100 epoxy-based negative photoresist (Kayaku Advanced Materials (former Microchem), Westborough, MA, USA) on the top of a conventional silicon wafer. The injection system was formed by replica molding of polydimethylsiloxane (PDMS, Sylgard 184, Dow Corning, Midland, MI, USA). To avoid the peel off and perforation, the PDMS fluidic system was bonded to the silicon chamber after chemical activation of their surfaces by oxygen plasma treatment (Diener Pico RIE, Ebhausen, Germany).

Design Considerations for the Membrane Reinforcement. Flow cells with membrane thicknesses of 2 and 5 μm were fabricated. Since the lateral size of the cell (5 mm by 20 mm) is large compared to the thickness of the membranes, they were reinforced using various backbone configurations, as shown in Figure 5. Each configuration was fabricated as shown in Figure 4. Surprisingly, the cells reinforced by ribs were found to be more fragile than the plane membranes without reinforcement and usually broke during filling with MQ water.

https://dx.doi.org/10.1021/acs.analchem.0c03763
Anal. Chem. XXXX, XXX, XXX−XXX

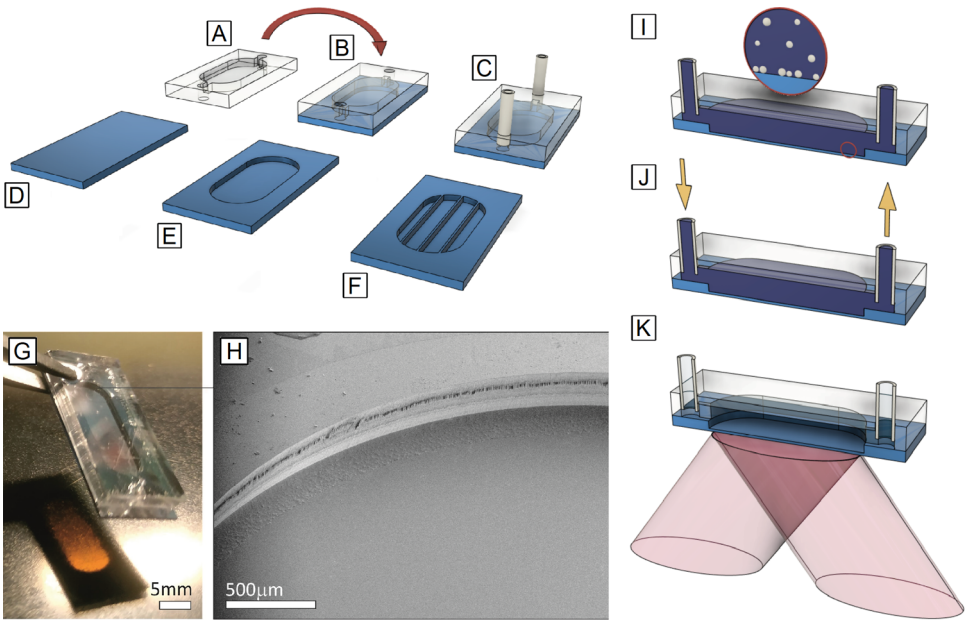

Figure 4. [A–F] Fabrication of a sealed chamber based on the membrane structure described in Figure 3 and the assembled flow cell with the thin (semitransparent) silicon membrane. [G] and [H] show the cell and the edge of the membrane. [I–K] Design of the membrane-based IRSE cell.

The cracks were developed along the edges between the ribs and the membrane (see Figure 5E,F). The membranes usually undulate slightly caused by the pressure of the sample depending on the injection process. The sample transport into the cells was tested in experimental setups of pressing the sample into or sucking from the chamber by both peristaltic and syringe pumps (see Figure 6 for the latter). Although the Si membranes are elastic and resistant against those deformations to some extent, the tests proved that, during these processes, cracks appear along the edges that lead to broken membranes very quickly. As a probable cause of the membrane deterioration, we can refer to the specific structure of the integrated flow cell. During the sealing process, the Si ribs were bonded to the covering PDMS layer. Accordingly, the ribs move together with the flexible PDMS contrariwise than the Si membrane and generate significant share stress at the connection edges during the injection process.

The 5 μm membranes without ribs proved to be the most stable mechanically, whereas the 2 μm cells were fragile even without the reinforcement ribs. Consequently, we used flow cells with 5 μm membranes without reinforcement in the further study. Note that the size of the cells was optimized for the large beam size and the small intensity of IRSE. However, more robust cells may be constructed by decreasing the size (causing an inevitable decrease of intensity by reducing the spot size), which can lead to the possibility of also using the 2 μm cell in the future, which will be the topic of a following study.

Mid-Infrared Spectroscopic Ellipsometry in a Membrane-Based Flow Cell. The micromachined flow cell (see Figures 3–5) was mounted on a vertical stage of the IR ellipsometer, as shown in Figure 6. The vertical position of the plane of the membrane is a significant advantage to avoid the formation of bubbles in water ambient. According to our previous experiences with conventional (through-the-water) flow cells, the horizontal location makes it hard to get rid of the bubbles that can possibly be generated during the *in situ* measurement at a location in the cell that is outside of the area

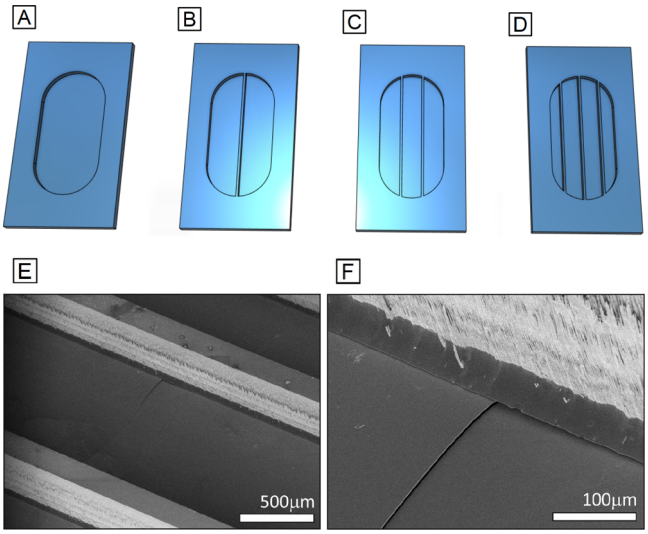

Figure 5. [A–D] Reinforcement patterns investigated in this study with an increasing number of ribs. SEM images [E] and [F] show the broken structures.

illuminated by the measurement beam. In the orientation shown in Figure 6, the bubbles are collected at the top of the cell.

The geometry of the stage allows that both the flow-in and flow-out tubes (Figure 4J) can be connected to the cell. In the configuration shown in Figure 6, a syringe pump is used to press the liquid into the cell. With this pump, the speed of flow can be adjusted and controlled in a careful way to avoid damaging the thin membrane of the cell.

The stage can be tilted and shifted, and the alignment is supported by a laser beam in the visible range. Once the rough alignment is established based on this beam, the final position was found by switching to IR illumination measuring the detected intensity real time while tilting and shifting the sample stage, as well as changing the spot size with an aperture. The spot size has to be decreased to make sure that the beam

https://dx.doi.org/10.1021/acs.analchem.0c03763
Anal. Chem. XXXX, XXX, XXX–XXX

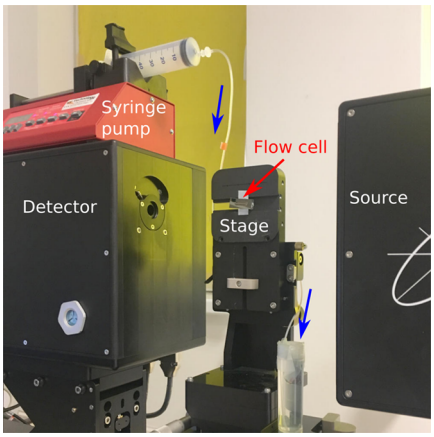

Figure 6. Photograph of the measurement setup showing the cell mounted on the vertical stage of the IR ellipsometer. The flow-in and flow-out tubes (see also Figure 4) are at the backside of the cell, pointing toward the plane of the image.

only covers the membrane (Figure 4K) and does not include that of the bulk wafer. Otherwise, the optical model would not be accurate, and the calculated spectra would not fit the measured ones.

In this configuration, the angle of incidence can be changed in a broad range, from below 45° to 90°. The advantage of smaller angles is that the elongation of the illuminated spot will be smaller. However, for many structures, the optimum condition that is close to the Brewster angle is usually larger. For larger angles, the spot might be needed to be reduced further in order to avoid the illumination of the sensor surface outside of the membrane and the cell (Figure 4K). The further advantage of a smaller spot is that, in the case of an inhomogeneously covered membrane surface, the properties within the illuminated area might be more uniform. Nevertheless, the trade-off between the spot size, the intensity, and the consistency cannot be avoided, and it requires careful considerations. Systematic measurements at different spot sizes might also be a preferable procedure, although in the case of IRSE, it takes a lot of time, and it can only be performed prior to the adsorption process.

The surface quality of the fabricated membranes were separately characterized by two AFMs (AIST-NT SmartSPM 1010, AIST_NT, Novato, CA, USA and XE-100 Psia, South Korea, NSC15 Micromash, Estonia) to verify the applicability of the optical model (Figure 2C). The results were reproducible with two different samples (with and without reinforcement). The outer surface of the membranes (silicon−air interface) is defined by the final chemo-mechanical polishing of the initial SOI wafer. Accordingly, the surfaces are smooth, having a root mean square (RMS) roughness of 0.25 nm. The inner surfaces of the membrane (sample−silicon interface) are formed by the epitaxial deposition of the silicon device layer on the buried oxide. In this case, the RMS is slightly higher, up to 0.65 nm (see Figure 3A−D).

According to the adequate optical quality of the membranes both the 2 and 5 μm membranes can be fitted using a simple model of (air as the ambient)/(oxide)/(c-Si as the layer)/(oxide)/(air as the substrate), using a thickness of 1.5 nm for the native oxide layer (see Figure 7 and the insets therein). However, in the case of the 2 μm membrane, a significant amount of lateral inhomogeneity has to be added to the model in order to achieve an acceptable fit quality (Figure 7A). It shows that the thickness of the 2 μm membrane has significant thickness deviations over the relatively large (≈20 mm long) illuminated area. In view of this fact, it is remarkable that the 5 μm membrane can perfectly be fitted without taking into account the lateral inhomogeneity in the optical model.

Figure 8 shows the calculated n and k (extinction coefficient) dispersions as well as the measured and fitted Ψ and Δ spectra after the PLGA adsorption. The difference between those spectra before and after the adsorption is shown in Figure 9A. There is a significant difference in both Ψ and Δ, multiple times larger than the noise. In the used measurement configuration, the standard deviations of both the measured Ψ and Δ ellipsometric angles are better than 0.5°, whereas the measured differences range up to 10°. The n and k spectra (Figure 9B,C) of the optical media in the system show a high

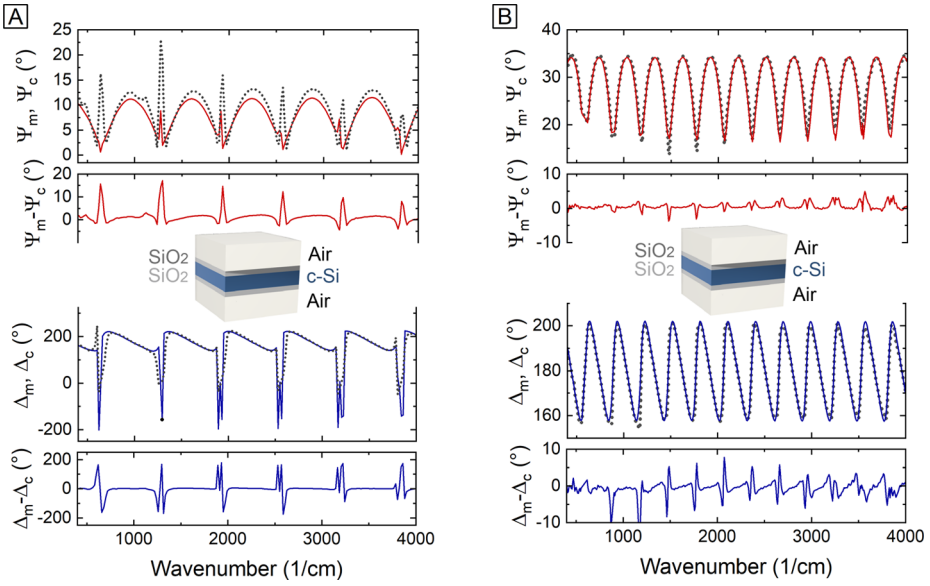

Figure 7. Measured (black dotted line) and fitted (colored lines) Ψ and Δ IR spectra on the 2 μm [A] and 5 μm [B] membranes before filling the cell. The inset shows the simple optical model with the thickness of the c-Si membrane being the only fit parameter.

https://dx.doi.org/10.1021/acs.analchem.0c03763
Anal. Chem. XXXX, XXX, XXX−XXX

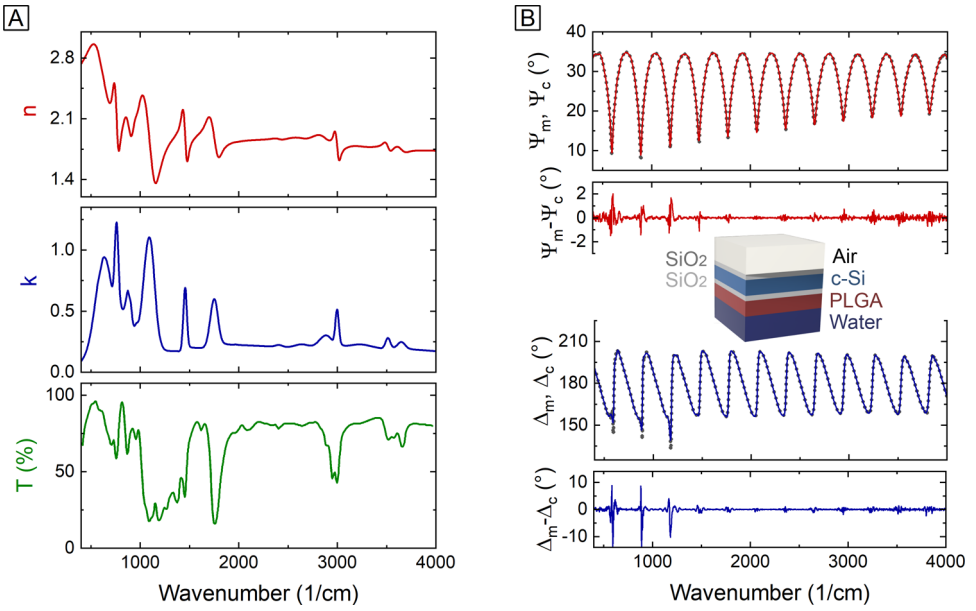

Figure 8. [A] n and k spectra determined from the evaluation shown in graph [B]. "T" denotes the transmission published in refs 25 and 26. The absorption band close to 1000 1/cm and around 1700 1/cm are associated with the vibration of C−O and carbonyl, respectively, whereas those between 2800 and 3000 1/cm are attributed to CH_2 and CH_3.[27] The peak at ≈1500 1/cm can be correlated with the C−O bond and the methyl group C−H bond (methyl group CH stretching) of PLGA.[28] Graph [B] shows the measured (black lines) and fitted (colored lines) spectra after PLGA nanoparticle adsorption. The differences are also plotted below the graphs.

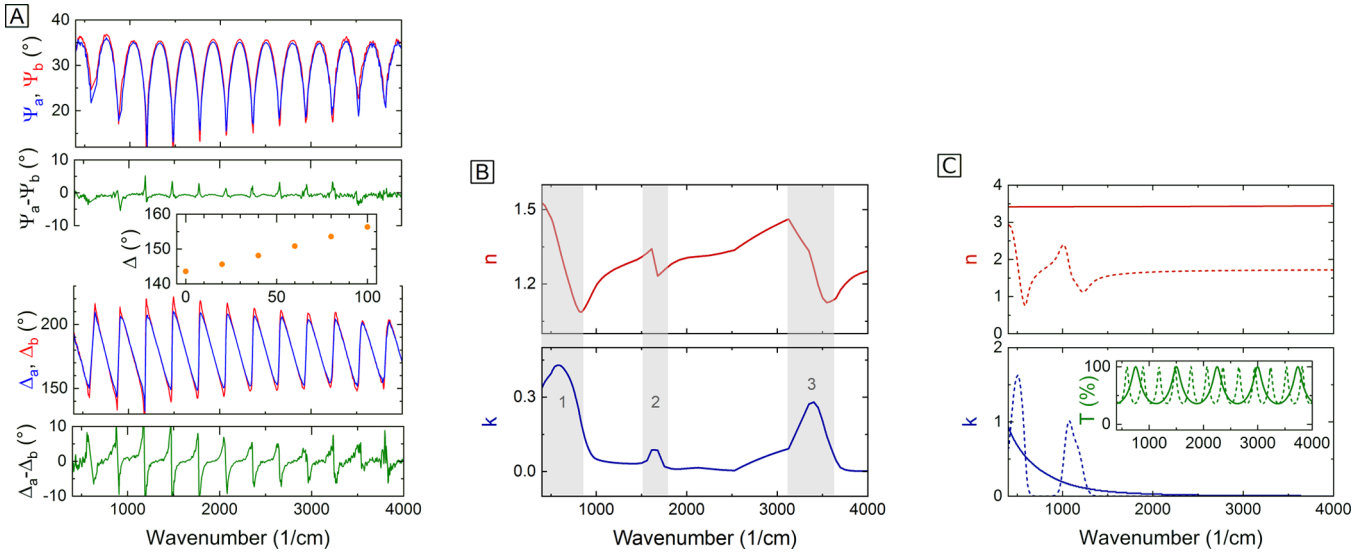

Figure 9. Ψ and Δ IR spectra measured on the 5 μm membrane before (red lines and index "b") and after (blue lines and index "a") the PLGA nanoparticle adsorption in water [A]. The inset in graph [A] shows the variation of Δ simulated at the wavenumber of 1473.5 1/cm as a function of the volume fraction (horizontal axis in percent) of PLGA under the 5 μm membrane. The error of the measurement is comparable to the symbol size in the inset of [A]. Graphs [B] and [C] show the n and k spectra of water[29] and membrane materials (Si, solid lines; and SiO_2, dashed lines), respectively, used for the evaluations. In graph [C], k of Si is multiplied by 10^4 for better visibility. The inset shows the transmission intensity for membrane thicknesses of 2 μm (solid line) and 5 μm (dashed line) at the angle of 53°.

contrast, whereas the transmission is acceptable in both membranes (see the inset of Figure 9C).

Evaluation and Sensitivity Analysis. The measured and fitted spectra are shown in Figure 8B with the optical model applied for the adsorption measurement. Here, the dry membrane model of Figure 7 was completed by a layer that describes the dispersion of PLGA using EMA with components of H_2O (see Figure 9B) and PLGA (V_{PLGA} = 23%) modeled using Gaussian oscillators (Figure 8).

The gradient fit was started using refs 25 and 26 as the initial position for the optical functions of PLGA. The thickness of the PLGA layer as a result of the Levenberg−Marquardt fit was 95 nm, which is in good agreement with the values obtained by the DLS and AFM methods. The uncertainties for the determination of volume fractions and thicknesses are typically 1% and a few nanometers, respectively. Figures 8A and 2E show the dispersions of n and k for PLGA and H_2O, respectively.

https://dx.doi.org/10.1021/acs.analchem.0c03763
Anal. Chem. XXXX, XXX, XXX−XXX

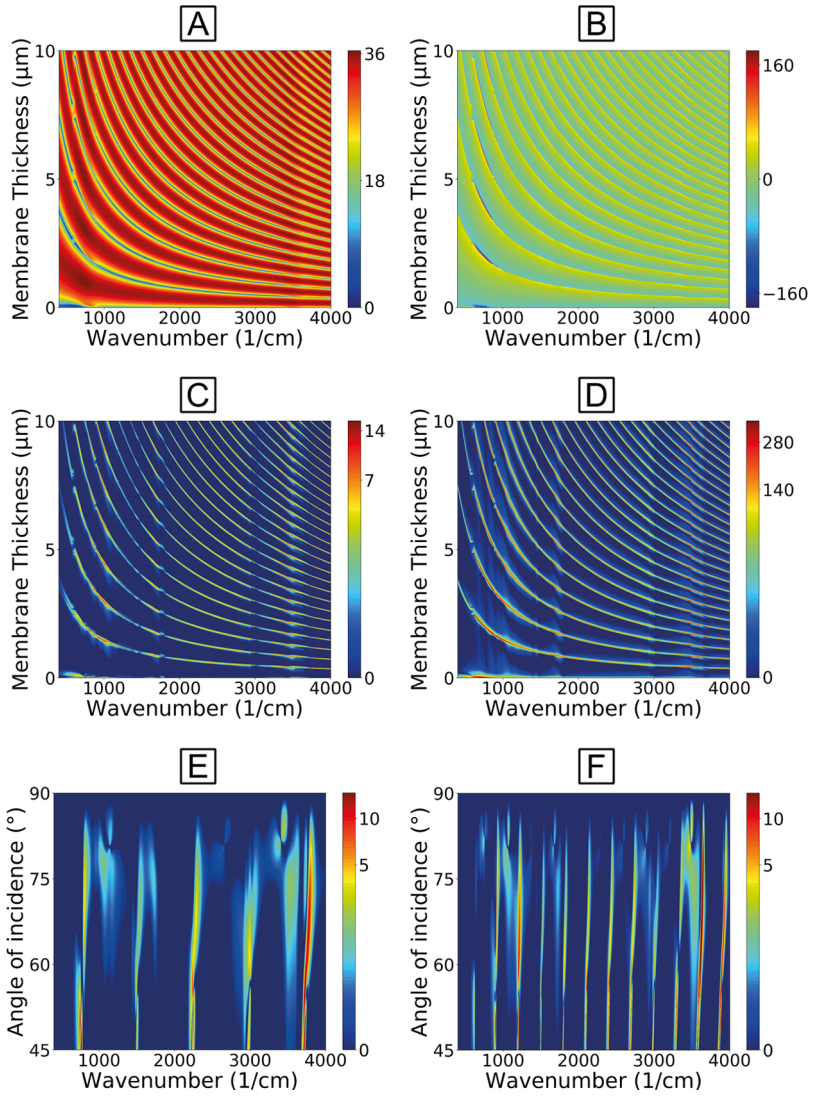

Figure 10. Simulated Ψ [A] and Δ [B] ellipsometric angles in the air/c-Si/water structure, the differences in Ψ [C] and Δ [D] before and after the PLGA adsorption for different membrane thicknesses as well as the differences in Ψ for the 2 μm [E] and the 5 μm [F] membrane before and after the PLGA adsorption for different angles and wavenumbers. The z-scale for graphs [C]−[F] is in $\log_{10}$ in order to amplify the structure in the range of small differences. Hence, the characteristic absorption bands (see Figure 8A) and the corresponding most sensitive angles can also be identified in this visualization. The n and k values of PLGA used in the simulation were determined from the fitted spectra of Figure 8B.

Ψ and Δ maps were calculated for membrane thicknesses from 0 to 10 μm and for wavenumbers from 400 to 4000 1/cm. Figure 10 shows the Ψ and Δ values without the PLGA layer (graphs [A] and [B]) as well as the difference with and without the PLGA layers (graphs [C] and [D]) in MQ water at an angle of incidence used for the measurement (53°). Due to the interference oscillations in the membrane, there are periodic positions of high sensitivity as a function of the wavenumber. The period decreases with increasing membrane thickness. For example, at the membrane thickness of 2 μm high-sensitivity positions can be found at wavenumbers of ≈750, ≈1500, ≈2250, ≈3000, and ≈3750 1/cm, whereas at the membrane thickness of 5 μm, the high-sensitivity positions are at ≈700, ≈1020, ≈1340, and so on, in steps of 320 1/cm.

The wavenumber positions of high sensitivities also depend on the angle of incidence, as shown in Figure 10E,F. The stripes of high sensitivity are only slightly shifted when changing the angle of incidence because the angle within the membrane and water changes less than in air. Note that it might even be better to use thicker membranes because, in that case, the number of high sensitivity positions is higher and, with the variation of the angle of incidence, these can cover a larger spectral area. Note that the low-transmission positions (Figure 9C) can also be shifted with the incident angle. This feature provides an opportunity to optimize the measurement for a certain absorption feature, depending on the investigated material or structure. In this work, there was no pre-selected target wavenumber to optimize for. Therefore, the main purpose of angle of incidence selection was to reduce the spot size, i.e., to use the smallest possible angle without a significant deterioration in sensitivity and intensity.

A further remarkable feature of the simulation and the measurements is that the low-wavenumber region is also accessible at high sensitivities. Note that not only the simulated sensitivity but also the measured intensity is high enough to provide precise measurement capabilities in the low-wavenumber region.[30]

https://dx.doi.org/10.1021/acs.analchem.0c03763
Anal. Chem. XXXX, XXX, XXX−XXX

DISCUSSION

IRSE in a Flow Cell. Figure 1 shows the optical properties of some IR-transparent materials in the wavelength range of 400−4000 1/cm that can potentially be used by most of the commercial IR ellipsometers. There are very few materials that are transparent all over this range (Figure 1), in which Si photonics is especially limited.[31] Besides transparency, there are other requirements that have to be met when fabricating a flow cell, such as the mechanical properties or chemical stability. For example, KBr offers the best optical properties; however, it is soluble in water, which is a serious disadvantage not only for flow cell applications but also because of the degradation by the humidity of air. Tiwald et al. used a ZnSe prism in a Kretschmann−Raether configuration that allowed access to the wavenumber range of ≈750−5500 1/cm.[13]

Most *in situ* IRSE solutions utilize highly transparent bulk materials in configurations that either enable the deflection of the light reflected from the outer surface of the cell[11] or ensure that there is no change of the ellipsometric angles, such as in the case of Kretschmann−Raether configurations.[13,32,33] The third possibility is to make a compromise with the given optical properties but using a thin-walled cell through which the absorption is acceptable. This leads to a microfabrication method described in the Microfabrication of a Membrane-Based Flow Cell for IRSE section that makes it possible to prepare a membrane cell with thicknesses down to a few microns. In this case, however, the mechanical properties also play a crucial role because the large area needed to achieve the required illumination intensity. The thin membrane can be critical regarding the pressure controlled injection of the sample. The stress-induced deviation in the optical properties could be a further issue considering pressure-dependent and flow rate-dependent membrane deformation.

The results of this study are promising regarding further improvement of the membrane-based cell concepts and proved that both the 2 and 5 μm cells were of high optical quality and mechanically stable without any rib reinforcement structures (Figures 4 and 5). In many cases, the ribs were even promoters of initial cracks (Figure 5) that developed during sample injection. Although the applied reinforcement structures were not proved to be applicable in our configuration, they can still be important when designing cells with even larger lateral sizes and thinner membranes. Note that the deposition of an adequate layer structure on the membrane can improve both the mechanical and optical characteristics, which has a large potential in the future. In the current configuration, no optical deviations were observed due to mechanical stress.

The membranes of the cells were stable in both pressing and sucking configurations with both peristaltic and syringe pumps; however, the flow cells were not systematically tested in a broad mechanical stress range, related to the alternating flow rate-induced and pressure-induced deformations. In general, the application of a syringe pump in a sucking configuration seemed to be the most comfortable solution considering the possible contamination of the parts and equipment.

Sealing by oxygen plasma enhanced bonding of PDMS and Si was robust during the *in situ* measurement. The flow cell as well as the PTFE tubes for sample injection and waste outlet were also persistent during the experiments.

Adsorption of PLGA Nanoparticles. The drawback of the membrane concept for *in situ* measurements is that the membrane structure with all its imperfections (non-uniformity of thickness and n, stress, roughness, oxide, surface contamination, deformation, etc.) must be considered in the optical model. These parameters, however, in general only influence the quantitation (typically in form of offsets) and not the sensitivity of the measurement. It means that the spectroscopic information can be obtained in spite of the aberrations.

The advantage of ellipsometry over IR spectroscopy is the ability to build optical models for the quantitative determination of structural parameters (volume fractions of phases, layer thicknesses, n, lateral and vertical inhomogeneities, etc.). In our case, the model includes the thickness of the membrane, the interface layers in forms of oxides and roughness, and the PLGA layer. The PLGA layer is a composition of water and V_{PLGA} = 23% PLGA. The n values of the nanoparticles were also fitted using the Cauchy dispersion of $n = A + B/\lambda^2$ with A and B as fitted model parameters in the visible range and using Gaussian oscillators for the absorption features in the mid-IR range. As a result, the intrinsic n dispersion of the PLGA nanoparticles were determined together with the other quantitative structural parameters in both the visible and IR wavelength ranges (see Figures 2E and 8A, respectively). In the IR region, however, the absorption bands related to chemical information help to distinguish between phases[34] that may hardly be separable in the visible region.

In the current investigation, the speed of the IRSE measurements was not pushed to the limits. The aim was to obtain spectra with low noise. Therefore, the real-time capabilities of the system were not utilized, only the fact that the layer formation can be measured *in situ*, in the liquid phase, right after the adsorption process. The dynamics of the adsorption process was determined from the visible range measurement (Figure 2D). The main parameters in addition to the intrinsic n determined for the PLGA layer were the volume fraction and the layer thickness. The values of these parameters were in good agreement with those from the visible-range SE and AFM (see Figure 2). In Figure 8A, the features of the optical spectra are compared to those published by ref 25 showing a good qualitative agreement.

Performance and Outlook. By proper optimizations, the duration of SE measurements in the visible range can be decreased down to ≈1 s for a whole spectrum. These parameters are in the range of minutes for IRSE even after optimization. The mathematical uncertainty of the quantitative parameters (such as the thickness and the volume fractions) from the Levenberg−Marquardt fit is typically a few percent, similar to that published by Sossna et al.[35] on stencil mask membranes. The noise is low enough to resolve absorptions related to chemical information. Especially important is that those features can also be resolved in the low-wavenumber region down to 400 1/cm. In the case of PLGA, most of the important absorption features are located in this low-wavenumber region.[30]

The lateral size of the cell was large enough to use the IR beam with only a little reduction in size. However, the results imply that membranes with even larger (greater than 20 mm by 5 mm) lateral dimensions can be prepared, especially when using thicker membranes or sophisticated reinforcement structures. Our measurements showed that the ribs did not deteriorate the possibilities for modeling. Their effect on the fit quality was negligible because the surface fraction of the rib area was small enough.

https://dx.doi.org/10.1021/acs.analchem.0c03763
Anal. Chem. XXXX, XXX, XXX−XXX

The angle of incidence and the spectral resolution vs speed and spot size can also be optimized further. The aim of this study was to demonstrate the applicability and performance of the method on a test material. Note that there are many opportunities in terms of both structural design and materials in the form of layers and membranes. Plasmonic,[36] waveguide,[37] 2D,[38] metamaterials,[39−41] and nanomaterials[42] as well as laterally varied[43] or multilayer[44,45] structures can also be fabricated on top or in place of the membrane resulting in complex optical responses that may be beneficial for enhanced effects in certain ranges of wavelengths or angles. Blending or focusing may also be an opportunity to achieve laterally resolved measurements, although the intensities are far from those available at synchrotron facilities[46] or by quantum cascade lasers[47,48] that, on the other hand, cover a narrower spectral range.

CONCLUSIONS

It was shown that flow cells for IRSE can be prepared using micromachined SOI wafers. The process includes lithography, metal sputtering, and DRIE processes on commercial SOI wafers. Membrane thicknesses of 2 and 5 μm were demonstrated; this can, however, be changed depending on the availability of the SOI wafers. It was shown that the lateral cell dimensions of 5 mm by 20 mm (a volume of 50 μL) can be realized without damaging the membranes during the liquid flow. The use of ribs for the reinforcement of the membranes is not beneficial, and they even increase the fragility of the structure because cracks can be developed at the edges between the ribs and the membrane. The fitted ellipsometry spectra revealed high-quality single-crystalline membranes, although those with a thickness of 2 μm were laterally inhomogeneous. The cells support measurements at angles of incidence limited only by the ellipsometer and a spectral range with wavenumbers down to 400 1/cm (wavelength of 25 μm) or even below (up to the wavelength of 30 μm, not utilized in this work). The applicability of the configuration was proved by *in situ* analysis of PLGA adsorption on the membrane surface. The characterization performance of the method was demonstrated by derivation of both chemical (bond states) and physical (layer thickness) properties of the nanoparticle layer. The concept presented in this work opens new opportunities, in which the thickness, the overlayers, the size, and many other parameters of the membrane cell can further be optimized in order to increase the sensitivity and speed and also to specifically adapt the performance to a certain spectral range that is important for a given task of detection or analysis.

AUTHOR INFORMATION

Corresponding Author

Peter Petrik − *Centre for Energy Research, H-1121 Budapest, Hungary;* orcid.org/0000-0002-5374-6952; Email: petrik.peter@energia.mta.hu

Authors

Alekszej Romanenko − *Centre for Energy Research, H-1121 Budapest, Hungary; Doctoral School of Chemistry, Eötvös Loránd University, H-1117 Budapest, Hungary*

Benjamin Kalas − *Centre for Energy Research, H-1121 Budapest, Hungary*

Petra Hermann − *Centre for Energy Research, H-1121 Budapest, Hungary*

Orsolya Hakkel − *Centre for Energy Research, H-1121 Budapest, Hungary*

Levente Illés − *Centre for Energy Research, H-1121 Budapest, Hungary*

Miklós Fried − *Centre for Energy Research, H-1121 Budapest, Hungary; Institute of Microelectronics and Technology, Óbuda University, H-1084 Budapest, Hungary*

Peter Fürjes − *Centre for Energy Research, H-1121 Budapest, Hungary*

Gergö Gyulai − *Laboratory of Interfaces and Nanostructures, Eötvös Loránd University, H-1117 Budapest, Hungary;* orcid.org/0000-0002-1352-2014

Complete contact information is available at: https://pubs.acs.org/10.1021/acs.analchem.0c03763

Author Contributions

A.R., P.F., G.G., and P.P. wrote the manuscript and prepared the figures. A.R., B.K., P.H., O.H., L.I., G.G., and P.P. worked on the experiments and evaluation. P.H., O.H., and P.F. prepared the devices. All authors reviewed the manuscript.

Notes

The authors declare no competing financial interest.

ACKNOWLEDGMENTS

Support from the National Development Agency grant of OTKA K131515, the ÚNKP-19-3 New National Excellence Program of the Ministry, and the M-ERA.NET "VOC-DETECT" project is greatly acknowledged. The work was partially supported by ENIAC JU and National Research, Development and Innovation Fund via the grant of ECSEL "Moore4Medical" (Nr. 876190) project. This work was completed in the ELTE Institutional Excellence Program (1783-3/2018/FEKUTSTRAT) and ELTE Thematic Excellence Programme (SZINT+) supported by the Hungarian Ministry for Innovation and Technology.

REFERENCES

(1) Palmer, R. A.; Smith, M. J. *Can. J. Phys.* **1986**, *64*, 1086−1092.

(2) van Soest, J. J. G.; Tournois, H.; de Wit, D.; Vliegenthart, J. F. G. *Carbohydr. Res.* **1995**, *279*, 201−214.

(3) Röseler, A. *Infrared Phys.* **1981**, *21*, 349−355.

(4) Schade, U.; Röseler, A.; Korte, E. H.; Bartl, F.; Hofmann, K. P.; Noll, T.; Peatman, W. B. *Rev. Sci. Instrum.* **2002**, *73*, 1568−1570. Publisher: American Institute of Physics

(5) Röseler, A.; Korte, E.-H. *Thin Solid Films* **1998**, *313-314*, 708−712.

(6) Korte, E. H.; Röseler, A. *Analyst* **1998**, *123*, 647−651 Publisher: The Royal Society of Chemistry.

(7) Tiwald, T. E.; Thompson, D. W.; Woollam, J. A.; Paulson, W.; Hance, R. *Thin Solid Films* **1998**, *313-314*, 661−666.

(8) Thompson, D. W.; DeVries, M. J.; Tiwald, T. E.; Woollam, J. A. *Thin Solid Films* **1998**, *313-314*, 341−346.

(9) Henrion, W.; Rebien, M.; Angermann, H.; Röseler, A. *Appl. Surf. Sci.* **2002**, *202*, 199−205.

(10) Hinrichs, K.; Röseler, A.; Gensch, M.; Korte, E. H. *Thin Solid Films* **2004**, *455-456*, 266−271.

(11) Mikhaylova, Y.; Ionov, L.; Rappich, J.; Gensch, M.; Esser, N.; Minko, S.; Eichhorn, K.-J.; Stamm, M.; Hinrichs, K. *Anal. Chem.* **2007**, *79*, 7676−7682.

(12) Aulich, D.; Hoy, O.; Luzinov, I.; Brücher, M.; Hergenröder, R.; Bittrich, E.; Eichhorn, K.-J.; Uhlmann, P.; Stamm, M.; Esser, N.; Hinrichs, K. *Langmuir* **2010**, *26*, 12926−12932. Publisher: American Chemical Society

(13) Tiwald, T. E.; Thompson, D. W.; Woollam, J. A.; Pepper, S. V. *Thin Solid Films* **1998**, *313-314*, 718−721.

(14) Gyulai, G.; Kiss, É. *J. Colloid Interface Sci.* **2017**, *500*, 9−19.
(15) Gyulai, G.; Pénzes, C. B.; Mohai, M.; Csempesz, F.; Kiss, É. *Eur. Polym. J.* **2013**, *49*, 2495−2503.
(16) Kozma, P.; Kozma, D.; Nemeth, A.; Jankovics, H.; Kurunczi, S.; Horvath, R.; Vonderviszt, F.; Fried, M.; Petrik, P. *Appl. Surf. Sci.* **2011**, *257*, 7160−7166.
(17) Kedenburg, S.; Vieweg, M.; Gissibl, T.; Giessen, H. *Opt. Mater. Express* **2012**, *2*, 1588−1611.
(18) Bruggeman, D. A. G. *Ann. Phys.* **1935**, *416*, 636.
(19) Herzinger, C. M.; Johs, B.; McGahan, W. A.; Woollam, J. A.; Paulson, W. *J. Appl. Phys.* **1998**, *83*, 3323−3336.
(20) Karagkiozaki, V.; Vavoulidis, E.; Karagiannidis, P.; Gioti, M.; Fatouros, D.; Vizirianakis, I.; Logothetidis, S. *Int. J. Nanomed.* **2012**, *7*, 5327−5338.
(21) Zhang, X.; Qiu, J.; Li, X.; Zhao, J.; Liu, L. *Appl. Opt.* **2020**, *59*, 2337−2344.
(22) Harendt, C.; Hunt, C. E.; Appel, W.; Graf, H.-G.; Höfflinger, B.; Penteker, E. *J. Electron. Mater.* **1991**, *20*, 267−277.
(23) Jastrzebski, L. *J. Cryst. Growth* **1984**, *70*, 253−270.
(24) Nguyen, B.-Y.; Celler, G.; Mazuré, C. *J. Intreg. Circuits Syst.* **2009**, *4*, 51.
(25) Jain, A.; Chasoo, G.; Singh, S. K.; Saxena, A. K.; Jain, S. K. *J. Microencapsulation* **2010**, *28*, 21−28.
(26) Jain, S.; Rathi, V. V.; Jain, A. K.; Das, M.; Godugu, C. *Nanomedicine* **2012**, *7*, 1311−1337.
(27) Xiao, H.; Wang, L. *Int. J. Nanomed.* **2015**, 5309.
(28) Labbaf, S.; Deb, S.; Cama, G.; Stride, E.; Edirisinghe, M. *J. Colloid Interface Sci.* **2013**, *409*, 245−254.
(29) Hale, G. M.; Querry, M. R. *Appl. Opt.* **1973**, *12*, 555−563.
(30) Kondyurin, A.; Kondyurina, I.; Bilek, M. Biodegradable drug eluting coating of cardiovascular stents dewets and can cause thrombosis. *arXiv:1101.0659 [cond-mat, physics:physics]* 2011, http://arxiv/org/abs/1101.0659.
(31) Soref, R. *Nat. Photonics* **2010**, *4*, 495−497. Number: 8 Publisher: Nature Publishing Group
(32) Kretschmann, E.; Raether, H. *Zeitschrift für Naturforschung A* **1968**, *23*, 615−617.
(33) Kalas, B.; Nador, J.; Agocs, E.; Saftics, A.; Kurunczi, S.; Fried, M.; Petrik, P. *Appl. Surf. Sci.* **2017**, *421*, 585−592.
(34) Kroning, A.; Furchner, A.; Aulich, D.; Bittrich, E.; Rauch, S.; Uhlmann, P.; Eichhorn, K.-J.; Seeber, M.; Luzinov, I.; Kilbey, S. M., II; Lokitz, B. S.; Minko, S.; Hinrichs, K. *ACS Appl. Mater. Interfaces* **2015**, *7*, 12430−12439.
(35) Sossna, E.; Kassing, R.; Rangelow, I. W.; Herzinger, C. M.; Tiwald, T. E.; Woollam, J. A.; Wagner, T. *Journal of Vacuum Science & Technology B: Microelectronics and Nanometer Structures Processing, Measurement, and Phenomena* **2000**, *18*, 3259−3263.
(36) Schwarz, B.; Reininger, P.; Ristanić, D.; Detz, H.; Andrews, A. M.; Schrenk, W.; Strasser, G. *Nat. Commun.* **2014**, *5*, 4085.
(37) Lin, P. T.; Kwok, S. W.; Lin, H.-Y. G.; Singh, V.; Kimerling, L. C.; Whitesides, G. M.; Agarwal, A. *Nano Lett.* **2014**, *14*, 231−238.
(38) Autore, M.; Li, P.; Dolado, I.; Alfaro-Mozaz, F. J.; Esteban, R.; Atxabal, A.; Casanova, F.; Hueso, L. E.; Alonso-González, P.; Aizpurua, J.; Nikitin, A. Y.; Vélez, S.; Hillenbrand, R. *Light: Science & Applications* **2018**, *7*, 17172−17172.
(39) Rodrigo, D.; Tittl, A.; Ait-Bouziad, N.; John-Herpin, A.; Limaj, O.; Kelly, C.; Yoo, D.; Wittenberg, N. J.; Oh, S.-H.; Lashuel, H. A.; Altug, H. *Nat. Commun.* **2018**, *9*, 2160.
(40) Shkondin, E.; Repän, T.; Aryaee Panah, M. E.; Lavrinenko, A. V.; Takayama, O. *ACS Applied Nano Materials* **2018**, *1*, 1212−1218.
(41) Folland, T. G.; Lu, G.; Bruncz, A.; Nolen, J. R.; Tadjer, M.; Caldwell, J. D. *ACS Photonics* **2020**, *7*, 614−621.
(42) Yang, X.; Sun, Z.; Low, T.; Hu, H.; Guo, X.; de Abajo, F. J. G.; Avouris, P.; Dai, Q. *Adv. Mater.* **2018**, *30*, 1704896.
(43) Kalas, B.; Zolnai, Z.; Sáfrán, G.; Serényi, M.; Agocs, E.; Lohner, T.; Nemeth, A.; Khánh, N. Q.; Fried, M.; Petrik, P. *Sci. Rep.* **2020**, *10*, 19266.
(44) Mayerhöfer, T. G.; Pahlow, S.; Popp, J. *NANO* **2020**, *9*, 741−760.
(45) Kalas, B.; Ferencz, K.; Saftics, A.; Czigany, Z.; Fried, M.; Petrik, P. *Appl. Surf. Sci.* **2021**, *536*, 147869.
(46) Roodenko, K.; Mikhaylova, Y.; Ionov, L.; Gensch, M.; Stamm, M.; Minko, S.; Schade, U.; Eichhorn, K.-J.; Esser, N.; Hinrichs, K. *Appl. Phys. Lett.* **2008**, *92*, 103102.
(47) Furchner, A.; Kratz, C.; Gkogkou, D.; Ketelsen, H.; Hinrichs, K. *Appl. Surf. Sci.* **2017**, *421*, 440−445.
(48) Furchner, A.; Kratz, C.; Hinrichs, K. *Opt. Lett.* **2019**, *44*, 4387−4390.

https://dx.doi.org/10.1021/acs.analchem.0c03763
Anal. Chem. XXXX, XXX, XXX−XXX